

Article

Effect of Cr³⁺ Doping on Magnetic Properties of Zn-Mg Ferrite Nanoparticles

Xiaogang Yu ^{1,2}, Renpeng Yang ¹, Chengwei Wu ¹, Bo Liu ² and Wei Zhang ^{1,*} 

¹ State Key Laboratory of Structural Analysis, Optimization and CAE Software for Industrial Equipment, Department of Engineering Mechanics, Dalian University of Technology, Dalian 116024, China

² School of Biomedical Engineering, Dalian University of Technology, Dalian 116024, China

* Correspondence: wei.zhang@dlut.edu.cn

Abstract: Zn_{0.6}Mg_{0.4}Cr_xFe_{2-x}O₄ (0 ≤ x ≤ 0.4) nanoparticles were synthesized using a hydrothermal technique. The obtained magnetic nanoparticles (MNPs) exhibited a spinel structure, where the lattice constant decreased with the Cr³⁺ ion content. The doping of Cr³⁺ ion (x = 0.1) increased the specific saturation magnetization to 46.4 emu/g but decreased to 20.0 emu/g with the further increase in the Cr³⁺ ion content to x = 0.4. The decrement in Curie temperature was ascribed to the weakened super-exchange interaction between the metal ions located at A-sites and B-sites, which arose from the doping of the Cr³⁺ ion. The T₂-weighted images gradually darkened with the increase in Zn_{0.6}Mg_{0.4}Cr_{0.1}Fe_{1.9}O₄ nanoparticles concentration, suggesting that the nanoparticles can enhance the image contrast. Zn_{0.6}Mg_{0.4}Cr_xFe_{2-x}O₄ (0 ≤ x ≤ 0.4) nanoparticles were able to heat the agar phantom to the hyperthermia temperature under the safe alternating magnetic field, which showed their potential in the magnetic induction hyperthermia.

Keywords: magnetic nanoparticles; Curie temperature; hyperthermia



Citation: Yu, X.; Yang, R.; Wu, C.; Liu, B.; Zhang, W. Effect of Cr³⁺ Doping on Magnetic Properties of Zn-Mg Ferrite Nanoparticles. *Magnetochemistry* **2023**, *9*, 181. <https://doi.org/10.3390/magnetochemistry9070181>

Academic Editor: Marian Grigoras

Received: 24 May 2023

Revised: 2 July 2023

Accepted: 6 July 2023

Published: 11 July 2023



Copyright: © 2023 by the authors. Licensee MDPI, Basel, Switzerland. This article is an open access article distributed under the terms and conditions of the Creative Commons Attribution (CC BY) license (<https://creativecommons.org/licenses/by/4.0/>).

1. Introduction

Spinel structured ferrite, one of the most crucial magnetic materials, is widely used in various practical applications from industrial to biomedical due to its high chemical stability and adjustable physical properties [1]. Among the spinel ferrite, Zn-Mg ferrite nanoparticles have gained significant interest. For example, Patil et al. [2] conducted an exploration of the use of Zn-Mg ferrite on humidity sensing applications. The application of magnetic nanoparticles (MNPs) depends on their physical properties, which are affected by the chemical composition and synthesis method [3]. Many researchers investigated the influence of cation replacement on the crystal structure and optical, electrical, and magnetic properties of Zn-Mg ferrite nanoparticles by doping divalent, trivalent, or rare earth cations [4–15]. However, the study on the effect of Cr³⁺ doping on the magnetic properties of Zn-Mg ferrite nanoparticles is limited. Mansour et al. [16] investigated the effect of Cr³⁺ ion doping on the elastic and magnetic properties of Zn_{0.2}Mg_{0.8}Cr_xFe_{2-x}O₄ (0 ≤ x ≤ 0.025) MNPs prepared via citrate–nitrate auto combustion. Haralka et al. [17] studied the substitution effect of Cr³⁺ ion on the structural, magnetic, and electrical properties of Zn_{0.5}Mg_{0.5}Cr_xFe_{2-x}O₄ (0 ≤ x ≤ 1.0) MNPs fabricated via sol–gel auto combustion. But they have not discussed the Curie temperature and heating efficiency, which are two critical parameters of MNPs for magnetic induction hyperthermia (MIH). The Curie temperature refers to the temperature at which ferro- or ferrimagnetic materials undergo a phase transition from ferro- or ferrimagnetic state to a paramagnetic state, which can be employed to self-regulate the hyperthermia temperature. Heating efficiency refers to the ability of MNPs to transform alternating magnetic field energy into heat energy, which affects the dosage of MNPs used in MIH [18]. It is known that the Curie temperature and heating efficiency are strongly dependent on the super-exchange interaction between the cations within MNPs and on the magnetic properties of MNPs, respectively [19], while the super-exchange

interaction and magnetic properties are affected by the chemical composition and synthesis method [3].

It has been reported that the $Zn_{0.6}Mg_{0.4}Fe_2O_4$ nanoparticles have the highest specific saturation magnetization among $Zn_xMg_{1-x}Fe_2O_4$ ($x = 0.2, 0.4, 0.6,$ and 0.8) nanoparticles synthesized via the hydrothermal method [20], which is beneficial for the MNPs to obtain a higher heating efficiency, as the heating efficiency is positively correlated with the specific saturation magnetization of MNPs [21]. Since the magnetic moment of the Cr^{3+} ion ($3 \mu_B$) is smaller than that of the Fe^{3+} ion ($5 \mu_B$), the replacement of the Fe^{3+} ion by the Cr^{3+} ion may decrease the super-exchange interaction and Curie temperature [21]. In addition, the Cr^{3+} ion has an analogous charge and radius with the Fe^{3+} ion, which allows the Cr^{3+} ion to be heavily doped into Zn-Mg ferrite without breaking its crystal structure and symmetry [22,23]. Therefore, in this paper, we synthesized $Zn_{0.6}Mg_{0.4}Cr_xFe_{2-x}O_4$ ($0 \leq x \leq 0.4$) MNPs using the hydrothermal method and investigated the impact of Cr^{3+} ion doping on the magnetic properties, Curie temperature, and heating efficiency.

2. Experiments

2.1. Materials

$FeCl_3 \cdot 6H_2O$ (AR), $CrCl_3 \cdot 6H_2O$ (AR), and NaOH (AR) were provided by Shanghai Aladdin Biochemical Technology Co., Ltd., Shanghai, China. $ZnCl_2$ (AR) and $MgCl_2 \cdot 6H_2O$ (AR) were provided by Shanghai Macklin Biochemical Co., Ltd., Shanghai, China. Agar powder was provided by Sigma-Aldrich (Shanghai) Trading Co., Ltd., Shanghai, China. All of the chemicals used were as-received.

2.2. Synthesis of Nanoparticles

The magnetic nanoparticles (MNPs) of $Zn_{0.6}Mg_{0.4}Cr_xFe_{2-x}O_4$ ($0 \leq x \leq 0.4$) were manufactured using hydrothermal technique. Firstly, 24 g sodium hydroxide was dissolved in 150 mL DI water to produce an alkaline solution, which is the precipitant agent. Then, 9.9 mmol $ZnCl_2$, 6.6 mmol $MgCl_2 \cdot 6H_2O$, and a total amount of 33.0 mmol $FeCl_3 \cdot 6H_2O$ and $CrCl_3 \cdot 6H_2O$ were mixed in 80 mL DI water to produce a clear metal ions solution. The molar ratios of $CrCl_3 \cdot 6H_2O$ and $FeCl_3 \cdot 6H_2O$ were 0:2, 0.1:1.9, 0.2:1.8, 0.3:1.7, and 0.4:1.6, corresponding to the MNPs of $Zn_{0.6}Mg_{0.4}Cr_xFe_{2-x}O_4$ ($x = 0, 0.1, 0.2, 0.3,$ and 0.4). After that, the precipitant agent prepared beforehand was added dropwise into the prepared metal ions solution at ambient temperature to obtain a precursor. The drop-adding process of precipitant was accompanied by magnetic stirring. Subsequently, the obtained precursor underwent a hydrothermal reaction at $300 \text{ }^\circ\text{C}$ for 6 h in a sealed autoclave. The hydrothermal reaction was accompanied by mechanical stirring at a rate of 250 rpm. After that, the autoclave was cooled to ambient temperature without any external intervention. The resulting precipitate was rinsed multiple times with deionized water and ethanol until neutral and then dried at $80 \text{ }^\circ\text{C}$ for 8 h to obtain $Zn_{0.6}Mg_{0.4}Cr_xFe_{2-x}O_4$ ($0 \leq x \leq 0.4$) nanoparticles.

2.3. Characterization

The geometrical dimension and crystalline structure of the MNPs were measured using transmission electron microscopy (TEM, FEI-Tecnaï G2 F30, FEI Co., Hillsboro, OR, USA). An X-ray powder diffractometer (XRD, Empyrean, Panalytical BV, Almelo, The Netherlands) was employed to capture the X-ray diffraction patterns to ascertain the crystalline structure of the MNPs. The magnetization curves were captured using a vibrating sample magnetometer (VSM, LakeShore 7400s, Lake Shore Cryotronics Inc., Columbus, OH, USA) at ambient temperature. The thermogravimetric curves of the prepared MNPs under a static magnetic field were captured on a thermogravimetric analyzer (TGA, Mettler Toledo SDTA851, Mettler Toledo GmbH, Schwarzenburg, Switzerland) to determine the Curie temperature. A nuclear magnetic resonance analyzer (Varian 400M NMR/MRI system, Varian Inc., Palo Alto, CA, USA) with a magnetic field of 0.5 T was employed to conduct magnetic resonance imaging (MRI) experiments and assess the performance of

MNPs as a contrast agent in MRI. The MNPs with different concentrations (0–0.88 mM) were dispersed in 0.8 wt.% agar gel for testing. The T_2 -weighted images were acquired by employing spin-echo imaging sequencing (TR = 4000 ms, TE = 24 ms) at room temperature. The parameters for measuring T_2 relaxation times were set to TW = 1000 ms, TE = 0.3 ms, NECH = 5000, and NS = 64. The prepared MNPs of 30 mg were added to a 1 mL agar solution with an agar content of 0.8 wt% to obtain a magnetic agar phantom. To characterize the magnetic heating capability of the MNPs, experiments on magnetic heating were carried out by subjecting the magnetic agar phantom to an alternating magnetic field (AMF, 32 kA/m, and 100 kHz). A fiberoptic thermometer was used to record the heating curve of the magnetic agar phantom.

3. Results and Discussion

3.1. Crystalline Structure and Morphology Analysis

Figure 1 exhibits XRD patterns of $Zn_{0.6}Mg_{0.4}Cr_xFe_{2-x}O_4$ ($0 \leq x \leq 0.4$) nanoparticles. The Bragg reflection peaks identified as crystal planes of (220), (311), (400), (422), (511), and (440) can be observed, which are the characteristic peaks of Fe_3O_4 , suggesting that the crystalline structures of the synthesized MNPs are cubic spinel structures. In addition, the characteristic peaks of $\alpha-Fe_2O_3$ are also observed in the MNPs without Cr^{3+} doping. But when Cr^{3+} is doped, the intensities of the characteristic peaks of $\alpha-Fe_2O_3$ decrease significantly. According to the XRD patterns, the contents of $\alpha-Fe_2O_3$ within $Zn_{0.6}Mg_{0.4}Cr_xFe_{2-x}O_4$ ($x = 0.0$ and 0.1) are calculated to be 48.9% and 6.2%, respectively. After the content of doped Cr^{3+} increases to $x = 0.2$, all the characteristic peaks of $\alpha-Fe_2O_3$ disappear, suggesting that there are almost no $\alpha-Fe_2O_3$ nanoparticles formed in the MNPs of $Zn_{0.6}Mg_{0.4}Cr_xFe_{2-x}O_4$ ($x = 0.2, 0.3$ and 0.4). The lattice constants of $Zn_{0.6}Mg_{0.4}Cr_xFe_{2-x}O_4$ ($x = 0.0, 0.1, 0.2, 0.3$, and 0.4), calculated using the formula of $a = d_{hkl} \sqrt{h^2 + k^2 + l^2}$ [24], are 8.4380 Å, 8.4186 Å, 8.4179 Å, 8.4160 Å, and 8.4090 Å, respectively, diminishing with the increment of Cr^{3+} ion. This decrement in lattice constant may be ascribed to the slight lattice shrinkage caused by the doping of Cr^{3+} , as the ionic radius of Cr^{3+} is smaller than that of Fe^{3+} (0.64 Å with respect to 0.67 Å) [21].

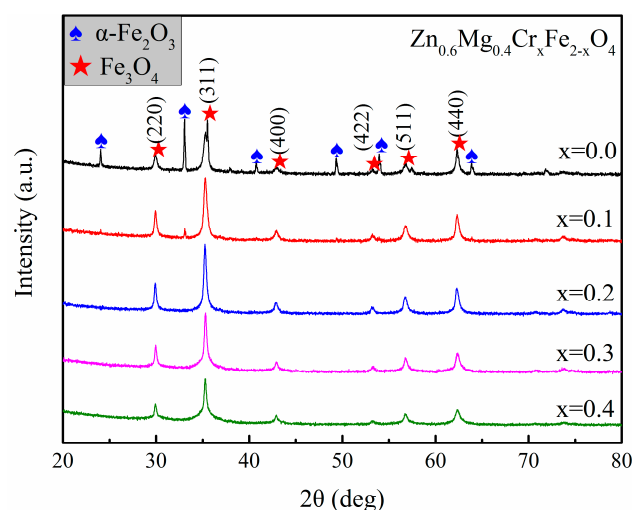


Figure 1. XRD diffraction patterns of $Zn_{0.6}Mg_{0.4}Cr_xFe_{2-x}O_4$ ($0 \leq x \leq 0.4$).

The TEM images of the fabricated MNPs in Figure 2 show that the prepared MNPs are composed of nanocubes accompanied by a few nanorods, as seen in Figure 2a,e, while the nanorods disappear in Figure 2i,m,q. The spinel ferrite nanoparticles synthesized under similar conditions usually are nanocubes [22,23], and the $\alpha-Fe_2O_3$ with the nanorod shape has also been reported by other literature [25,26]. Combined with the XRD patterns displayed in Figure 1, it can be inferred that the nanocubes are $Zn_{0.6}Mg_{0.4}Cr_xFe_{2-x}O_4$ ($0 \leq x \leq 0.4$), while the nanorods may be the $\alpha-Fe_2O_3$ particles. The size distribution

histograms of $\text{Zn}_{0.6}\text{Mg}_{0.4}\text{Cr}_x\text{Fe}_{2-x}\text{O}_4$ ($x = 0, 0.1, 0.2, 0.3,$ and 0.4) are displayed in Figure 2b, 2f, 2j, 2n, and 2r, showing that the size distributions obey the lognormal distribution. The average sizes of $\text{Zn}_{0.6}\text{Mg}_{0.4}\text{Cr}_x\text{Fe}_{2-x}\text{O}_4$ ($x = 0, 0.1, 0.2, 0.3,$ and 0.4) are 31.9 nm, 43.7 nm, 59.3 nm, 85.8 nm, and 101.9 nm, respectively, increasing with the Cr^{3+} content. The replacement of the Fe^{3+} ion by the Cr^{3+} ion causes an increment in the total ion content of the reaction solution, leading to an acceleration in ion diffusion and an increment in particle size [21]. The increase in spinel ferrite nanoparticles size with Cr^{3+} ion content is also observed in other literature [23]. Figure 2c,g,k,o,s are high-resolution TEM images of the MNPs, in which the lattice fringes are distinctly visible. The lattice fringe spacings are determined to be 0.489 nm, 0.491 nm, 0.304 nm, 0.265 nm, and 0.508 nm, which are consistent with the (111), (111), (220), (311), and (111) planes of spinel ferrite. Figure 2d,h,l,p,t exhibit the electron diffraction images of $\text{Zn}_{0.6}\text{Mg}_{0.4}\text{Cr}_x\text{Fe}_{2-x}\text{O}_4$ ($x = 0, 0.1, 0.2, 0.3,$ and 0.4), in which the diffraction rings can be identified as the crystal planes of (220), (311), (400), (511), and (440), which are the five main crystal planes of spinel ferrite. These results further confirm that the crystalline structures of the synthesized MNPs are spinel structures.

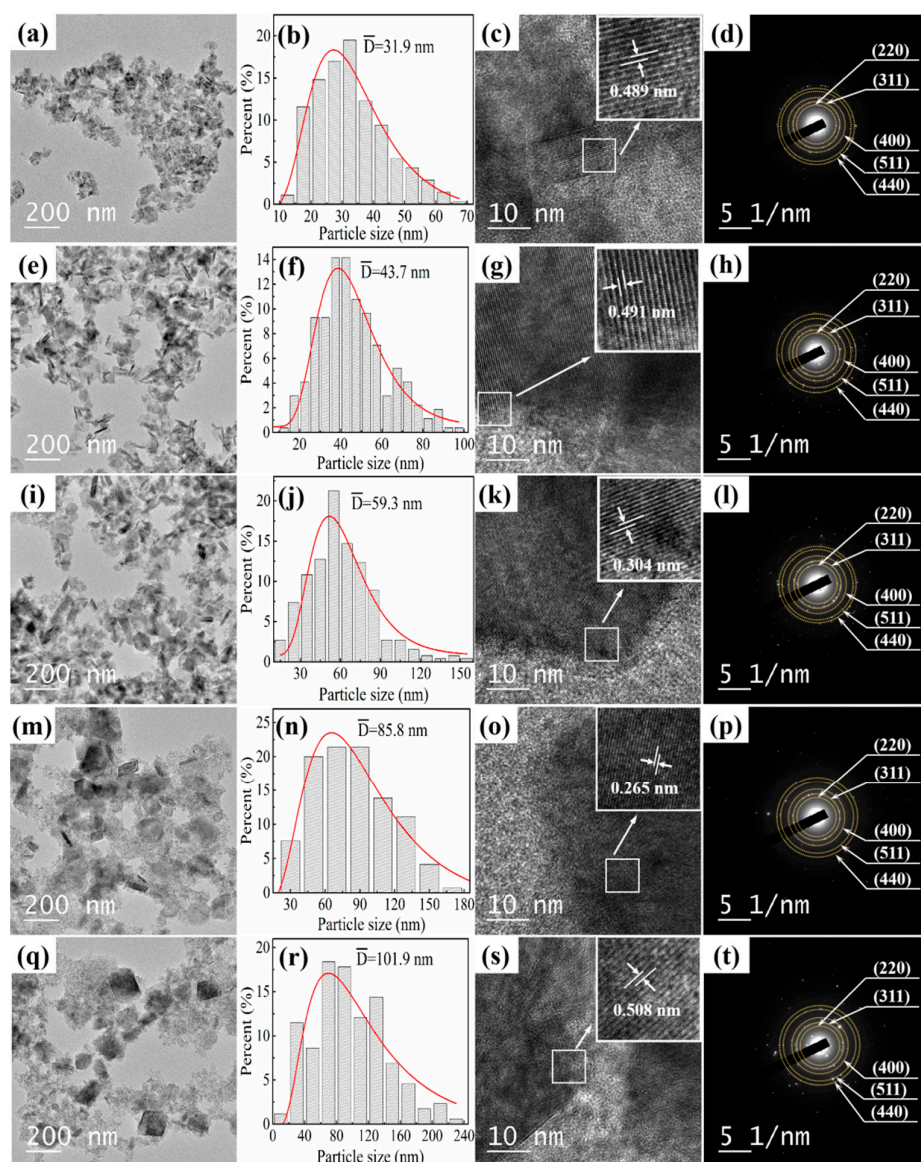


Figure 2. TEM micrographs, size distributions, high-resolution TEM images, and electron diffraction images of $\text{Zn}_{0.6}\text{Mg}_{0.4}\text{Cr}_x\text{Fe}_{2-x}\text{O}_4$ ($0 \leq x \leq 0.4$). (a–d) for $x = 0$, (e–h) for $x = 0.1$, (i–l) for $x = 0.2$, (m–p) for $x = 0.3$, (q–t) for $x = 0.4$.

3.2. Magnetic Properties

Figure 3a shows the magnetization curves of $\text{Zn}_{0.6}\text{Mg}_{0.4}\text{Cr}_x\text{Fe}_{2-x}\text{O}_4$ ($0 \leq x \leq 0.4$) at room temperature. The typically sigmoidal magnetization curves of superparamagnetic nanoparticles can be observed [27], suggesting that the synthesized MNPs are superparamagnetic. The measured specific saturation magnetization of $\text{Zn}_{0.6}\text{Mg}_{0.4}\text{Cr}_x\text{Fe}_{2-x}\text{O}_4$ ($x = 0.0, 0.1, 0.2, 0.3,$ and 0.4) are 32.2 emu/g, 46.1 emu/g, 40.8 emu/g, 28.8 emu/g, and 20.0 emu/g, respectively. The smaller σ_s of $\text{Zn}_{0.6}\text{Mg}_{0.4}\text{Cr}_x\text{Fe}_{2-x}\text{O}_4$ ($x = 0.0$) may be attributed to the existence of $\alpha\text{-Fe}_2\text{O}_3$ (as shown in the XRD pattern in Figure 1). It is known that $\alpha\text{-Fe}_2\text{O}_3$ is a canted antiferromagnet, in which the magnetization is marginal at room temperature. Thus, the true specific saturation magnetization of $\text{Zn}_{0.6}\text{Mg}_{0.4}\text{Cr}_x\text{Fe}_{2-x}\text{O}_4$ ($x = 0.0$ and 0.1) can be calculated by dividing the measured values by the percentages of their mass (51.1% and 93.8%, respectively). The true specific saturation magnetization of $\text{Zn}_{0.6}\text{Mg}_{0.4}\text{Cr}_x\text{Fe}_{2-x}\text{O}_4$ ($x = 0.0$ and 0.1) is calculated to be 63.0 emu/g and 49.1 emu/g, as shown in Figure 3b. It is apparent that the specific saturation magnetization of $\text{Zn}_{0.6}\text{Mg}_{0.4}\text{Cr}_x\text{Fe}_{2-x}\text{O}_4$ ($0 \leq x \leq 0.4$) decreases linearly with the increment of Cr^{3+} concentration.

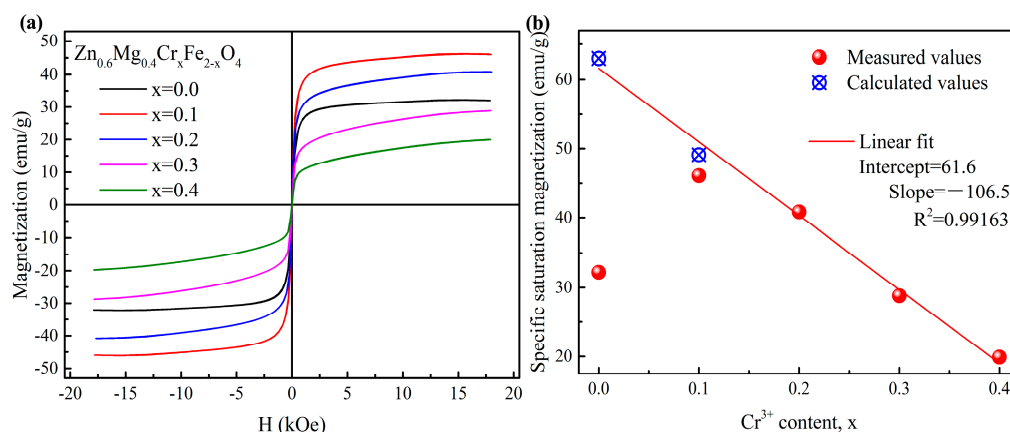


Figure 3. (a) The magnetization curves of $\text{Zn}_{0.6}\text{Mg}_{0.4}\text{Cr}_x\text{Fe}_{2-x}\text{O}_4$ ($0 \leq x \leq 0.4$) at room temperature and (b) the variation in specific saturation magnetization in relation to the concentration of Cr^{3+} ion.

It is well established that the magnetization exhibited by MNPs results from the organized alignment of their magnetic moments. The magnetic order in spinel ferrite is primarily produced via magnetic interactions between the cations located at the tetrahedral site (A site) and octahedral site (B site). The greatest interaction, known as the A – B interaction, occurs between the cations located at A sites and B sites. The B – B interaction is weaker, whereas the weakest is the A – A interaction [28].

As per Neel's sub-lattice model, the total magnetic moment exhibited by each formula unit in the spinel ferrite MNPs with the A – B interaction dominant is equal to the difference between the total magnetic moments at A -sites (M_A) and B -sites (M_B) with a unit of Bohr magneton (μ_B) [29,30]. Therefore, the specific saturation magnetization (σ_s) can be calculated using Formula (1) as follows:

$$\sigma_s = \frac{5585(M_B - M_A)}{M_w} \quad (1)$$

where M_w indicates the molecular weight of the MNPs. Due to the strong tendency of the Cr^{3+} ion to occupy B sites, the doped Cr^{3+} ion ($3 \mu_B$) will replace the Fe^{3+} ions ($5 \mu_B$) at B sites, causing a decrement in the total magnetic moment on the B sites, which, in turn, results in the decrement of specific saturation magnetization.

3.3. Curie Temperature

Curie temperature (T_c) is a critical temperature of magnetic materials, below which the magnetic moments within the magnetic materials will be ordered, and the materials

will exhibit a fairly strong magnetization. Once the temperature of magnetic materials goes above the critical temperature, the ordered magnetic moments within the materials will become disordered, and the magnetization will be reduced to such a tiny value that usually can be ignored compared with ferro- or ferrimagnetic ones [18]. To examine the impact of Cr^{3+} ion doping on the Curie temperature of $\text{Zn}_{0.6}\text{Mg}_{0.4}\text{Cr}_x\text{Fe}_{2-x}\text{O}_4$ ($0 \leq x \leq 0.4$) nanoparticles, the thermogravimetric curves of the samples are given in Figure 4. Curie temperature is taken as the temperature at which the thermogravimetric curve attains its maximum first derivative [31,32], as shown in the insets of Figure 4. The Curie temperatures of $\text{Zn}_{0.6}\text{Mg}_{0.4}\text{Cr}_x\text{Fe}_{2-x}\text{O}_4$ ($x = 0.0, 0.1, 0.2, 0.3,$ and 0.4) are 180.0°C , 162.5°C , 150.5°C , 140.8°C , and 124.8°C , respectively, dropping off linearly with the increment of the Cr^{3+} ion concentration, as exhibited in Figure 4f. It is recognized that the ordered orientation of the magnetic moments within the spinel ferrite is the result of the super-exchange interaction that occurs between the cations located at *A*-sites and *B*-sites, which causes the Curie temperature to positively correlate with the super-exchange interaction between the cations posited at *A* and *B* sites [19]. As the magnetic moment of the Cr^{3+} ion is smaller than that of the Fe^{3+} ion ($3 \mu_B$ compared to $5 \mu_B$), the substitution of the Fe^{3+} ion for the Cr^{3+} ion will result in a decrease in the *A*–*B* super-exchange interaction, which ultimately causes a reduction in Curie temperature [21].

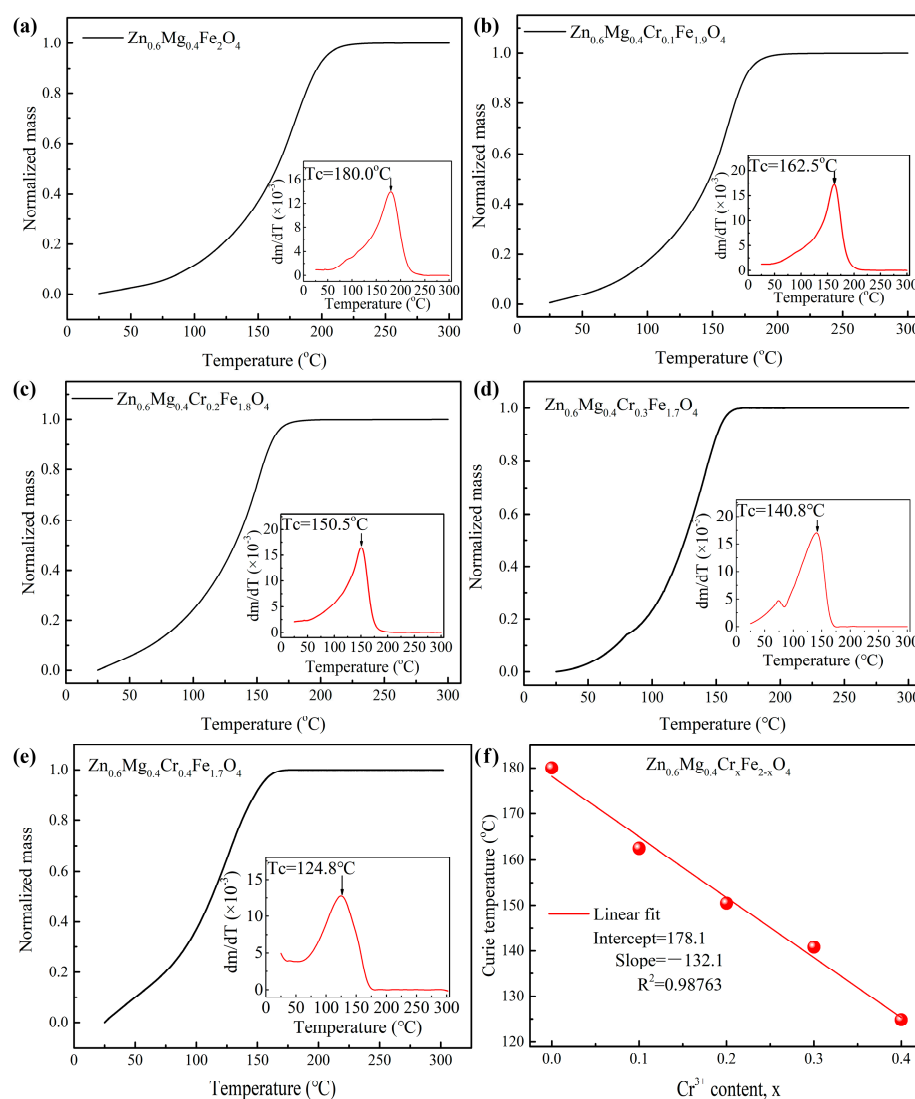


Figure 4. The thermogravimetric curves of $\text{Zn}_{0.6}\text{Mg}_{0.4}\text{Cr}_x\text{Fe}_{2-x}\text{O}_4$ ($0 \leq x \leq 0.4$) under a static magnetic field (a–e) and the Curie temperature variation versus the Cr^{3+} content (f).

3.4. Magnetic Resonance Imaging Experiments

Magnetic resonance imaging (MRI) is an imaging technique with the advantages of being noninvasive, non-ionizing, and radiation free, which is widely used in clinical diagnosis. The generation of images relies on the differences between the spin–lattice relaxation (T_1) time and the spin–spin relaxation (T_2) time of hydrogen protons in different tissues [33]. In order to enhance the imaging contrast and resolution, MRI is usually used in conjunction with contrast agents. As MNPs can generate a localized magnetic field to shorten the T_2 relaxation time of hydrogen protons in the vicinity, they usually serve as contrast agents in MRI [34]. To assess the potential application of synthesized MNPs in MRI, the T_2 -weighted images arising from $\text{Zn}_{0.6}\text{Mg}_{0.4}\text{Cr}_{0.1}\text{Fe}_{1.9}\text{O}_4$ nanoparticles are measured, as the MRI performance of MNPs is positively correlated with their specific saturation magnetization [35]. As shown in the inset of Figure 5, the T_2 -weighted images gradually darken with the $\text{Zn}_{0.6}\text{Mg}_{0.4}\text{Cr}_{0.1}\text{Fe}_{1.9}\text{O}_4$ nanoparticles concentration. The T_2 relaxation, also called spin–spin relaxation, refers to a decay in transverse magnetization resulting from a combination of spin–spin relaxation and magnetic field inhomogeneity [36]. When an external magnetic field is applied, MNPs will generate local inhomogeneity in the magnetic field, shortening the T_2 relaxation time and reducing the gray value of T_2 -weighted images. To quantitatively characterize the performance of $\text{Zn}_{0.6}\text{Mg}_{0.4}\text{Cr}_{0.1}\text{Fe}_{1.9}\text{O}_4$ nanoparticles as a contrast agent for MRI, the T_2 relaxation time is measured. Since T_2 relaxation time is a relative value, which will change with the concentration of applied MNPs, the relaxation rate R_2 , equal to the ratio of $1/T_2$ relaxation time to MNPs concentration by a linear fit, is usually used to describe the performance of MNPs as a contrast agent for MRI [37]. As seen in Figure 5, the relaxation rate R_2 of $\text{Zn}_{0.6}\text{Mg}_{0.4}\text{Cr}_{0.1}\text{Fe}_{1.9}\text{O}_4$ nanoparticles is calculated to be $74.48 \text{ mM}^{-1}\cdot\text{s}^{-1}$, which is higher than the reported value of $35.92 \text{ mM}^{-1}\cdot\text{s}^{-1}$ [38], suggesting that the synthesized $\text{Zn}_{0.6}\text{Mg}_{0.4}\text{Cr}_{0.1}\text{Fe}_{1.9}\text{O}_4$ nanoparticles possess the potential application in MRI.

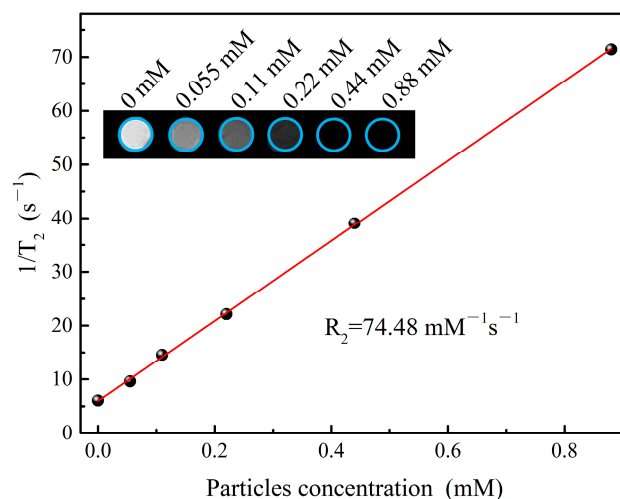


Figure 5. Linear fitting of $1/T_2$ of $\text{Zn}_{0.6}\text{Mg}_{0.4}\text{Cr}_{0.1}\text{Fe}_{1.9}\text{O}_4$ nanoparticles. The inset is the T_2 -weighted images.

3.5. Magnetic Heating Experiments

Figure 6a exhibits the magnetic heating curves of the agar phantom containing MNPs at a concentration of 30 mg/mL. It can be seen that once the AMF (32 kA/m , 100 kHz , below the safety threshold of $5 \times 10^9 \text{ A}\cdot\text{m}^{-1}\cdot\text{s}^{-1}$ [39]) is applied, the temperatures of the magnetic agar phantoms rise rapidly and exceed $42 \text{ }^\circ\text{C}$ after about 25 min. This suggests that the MNPs of $\text{Zn}_{0.6}\text{Mg}_{0.4}\text{Cr}_x\text{Fe}_{2-x}\text{O}_4$ ($0 \leq x \leq 0.4$) have good magnetic heating properties and possess the potential to be used in magnetic induction hyperthermia.

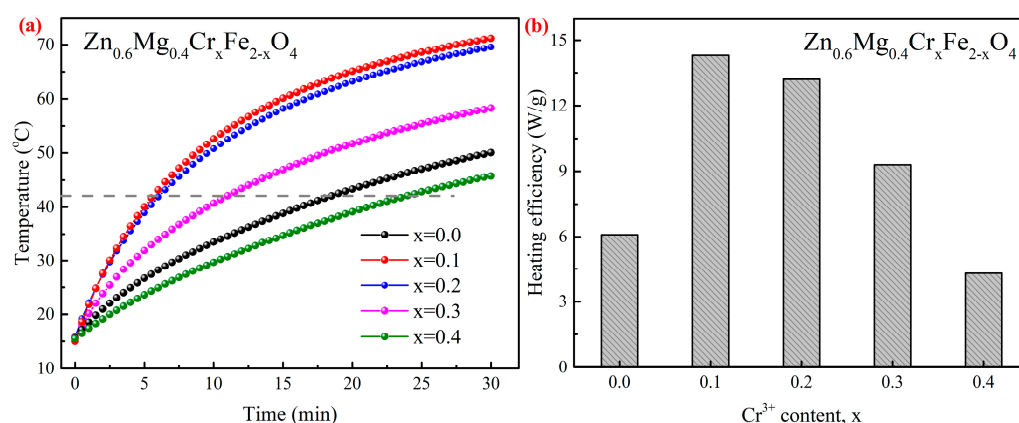


Figure 6. (a) The magnetic heating curves of MNPs agar phantom under an AMF of 32 kA/m and 100 kHz. (b) The changes in heating efficiency of $\text{Zn}_{0.6}\text{Mg}_{0.4}\text{Cr}_x\text{Fe}_{2-x}\text{O}_4$ ($0 \leq x \leq 0.4$) against the Cr^{3+} content.

Generally, the heating efficiency, i.e., the amount of heat converted per unit mass of MNPs in per unit time from electromagnetic field energy, is expressed as specific loss power (SLP) with a unit of W/g, which can be calculated via Formula (2) as follows [40]:

$$SLP = C \frac{m_a}{m_p} \frac{dT}{dt} \Big|_{t \rightarrow 0} \quad (2)$$

where m_p denotes the mass of the MNPs within the magnetic agar phantom, m_a indicates the mass of the magnetic agar phantom, $dT/dt|_{t \rightarrow 0}$ represents the initial slope of the magnetic heating curve, and C is the specific heat capacity of the magnetic agar phantom, which can be approximated as $4.2 \text{ J} \cdot \text{g}^{-1} \cdot \text{°C}^{-1}$ [41]. Based on the experimental evidence presented in Figure 6a, the SLP of $\text{Zn}_{0.6}\text{Mg}_{0.4}\text{Cr}_x\text{Fe}_{2-x}\text{O}_4$ ($x = 0.0, 0.1, 0.2, 0.3$ and 0.4) are 6.1 W/g, 14.3 W/g, 13.2 W/g, 9.3 W/g, and 4.3 W/g, respectively, under the AMF of 32 kA/m and 100 kHz, as exhibited in Figure 6b. The heating efficiency of the prepared MNPs increases initially and then decreases with the increasing concentration of doped Cr^{3+} ion. This trend is in line with the variation observed in the measured specific saturation magnetization as demonstrated in Figure 3b since the heating efficiency is directly linked to the specific saturation magnetization of the materials [42].

4. Conclusions

The $\text{Zn}_{0.6}\text{Mg}_{0.4}\text{Cr}_x\text{Fe}_{2-x}\text{O}_4$ ($0 \leq x \leq 0.4$) nanoparticles with spinel structures are successfully prepared using the hydrothermal technique, and the impact of Cr^{3+} ion doping on the geometric size, crystal structure, magnetic properties, Curie temperature, and magnetic heating properties are investigated. The results suggest that with the increase in the concentration of Cr^{3+} ion, $\text{Zn}_{0.6}\text{Mg}_{0.4}\text{Cr}_x\text{Fe}_{2-x}\text{O}_4$ ($0 \leq x \leq 0.4$) nanoparticles exhibit an increase in average size from 31.9 nm to 101.9 nm, and a decrease in lattice constant from 8.4380 Å to 8.4090 Å. The actual specific saturation magnetization of the prepared samples decreased linearly with the increment of Cr^{3+} concentration, which was attributed to the strong tendency of Cr^{3+} ions to occupy the B sites. The substitution of Fe^{3+} ions ($5 \mu_B$) for Cr^{3+} ion, which has weaker magnetic moments ($3 \mu_B$), caused a decline in the super-exchange interaction between the cations located at A-sites and B-sites. This, in turn, caused a decrement in the Curie temperature from 180.0 °C to 124.8 °C. The T_2 -weighted images arising from $\text{Zn}_{0.6}\text{Mg}_{0.4}\text{Cr}_{0.1}\text{Fe}_{1.9}\text{O}_4$ nanoparticles gradually darkened with the increase in MNPs concentration. The relaxation rate R_2 was $74.48 \text{ mM}^{-1} \cdot \text{s}^{-1}$, showing the potential application of $\text{Zn}_{0.6}\text{Mg}_{0.4}\text{Cr}_{0.1}\text{Fe}_{1.9}\text{O}_4$ nanoparticles as a contrast agent in MRI. On account of the influence of the measured specific saturation magnetization, the magnetic heating efficiency of $\text{Zn}_{0.6}\text{Mg}_{0.4}\text{Cr}_x\text{Fe}_{2-x}\text{O}_4$ ($0 \leq x \leq 0.4$) increased initially and then decreased. After the application of AMF for 25 min, the temperatures of the magnetic

agar phantoms rapidly rose to the hyperthermia temperature, exhibiting the potential of $\text{Zn}_{0.6}\text{Mg}_{0.4}\text{Cr}_x\text{Fe}_{2-x}\text{O}_4$ ($0 \leq x \leq 0.4$) to be used in magnetic induction hyperthermia.

Author Contributions: Conceptualization, X.Y. and W.Z.; methodology, X.Y. and R.Y.; software, X.Y.; validation, X.Y. and R.Y.; investigation, X.Y. and R.Y.; resources, X.Y.; data curation, X.Y. and R.Y.; writing—original draft, X.Y.; writing—review and editing, X.Y., R.Y., B.L. and W.Z.; visualization, X.Y.; supervision, B.L., C.W. and W.Z.; project administration, C.W. and W.Z.; funding acquisition, C.W. and W.Z. All authors have read and agreed to the published version of the manuscript.

Funding: This work was supported by the National Key Research and Development Project of China (2022YFE0115400, 2018YFA0704103, 2018YFA0704104), Fundamental Research Funds for the Central Universities (DUT21TD105, DUT22YG123), and Spring Sunshine Program (HZKY20220413).

Institutional Review Board Statement: Not applicable.

Informed Consent Statement: Not applicable.

Data Availability Statement: The data are available upon request.

Conflicts of Interest: The authors declare no conflict of interest.

References

- Somvanshi, S.B.; Khedkar, M.V.; Kharat, P.B.; Jadhav, K.M. Influential Diamagnetic Magnesium (Mg^{2+}) Ion Substitution in Nano-Spinel Zinc Ferrite (ZnFe_2O_4): Thermal, Structural, Spectral, Optical and Physisorption Analysis. *Ceram. Int.* **2020**, *46*, 8640–8650.
- Patil, S.N.; Pawar, A.M.; Tilekar, S.K.; Ladgaonkar, B.P. Investigation of Magnesium Substituted Nano Particle Zinc Ferrites for Relative Humidity Sensors. *Sens. Actuators A-Phys.* **2016**, *244*, 35–43.
- Hashim, M.; Alimuddin; Kumar, S.; Shirsath, S.E.; Kotnala, R.K.; Shah, J.; Kumar, R. Influence of Cr^{3+} Ion on the Structural, AC Conductivity and Magnetic Properties of Nanocrystalline Ni-Mg Ferrite. *Ceram. Int.* **2013**, *39*, 1807–1819. [[CrossRef](#)]
- Sharma, R.; Thakur, P.; Kumar, M.; Barman, P.B.; Sharma, P.; Sharma, V. Enhancement in A-B Super-Exchange Interaction with Mn Substitution in Mg-Zn Ferrites as a Heating Source in Hyperthermia Applications. *Ceram. Int.* **2017**, *43*, 13661–13669. [[CrossRef](#)]
- Mohseni, H.; Shokrollahi, H.; Sharifi, I.; Gheisari, K.H. Magnetic and Structural Studies of the Mn-Doped Mg-Zn Ferrite Nanoparticles Synthesized by the Glycine Nitrate Process. *J. Magn. Magn. Mater.* **2012**, *324*, 3741–3747.
- Ansari, M.; Bigham, A.; Hassanzadeh Tabrizi, S.A.; Abbastabar Ahangar, H. Copper-Substituted Spinel Zn-Mg Ferrite Nanoparticles as Potential Heating Agents for Hyperthermia. *J. Am. Ceram. Soc.* **2018**, *101*, 3649–3661.
- Gangaswamy, D.R.S.; Bharadwaj, S.; Chaitanya Varma, M.; Choudary, G.; Rao, K.H. Unusual Increase in Permeability in Cobalt Substituted Ni-Zn-Mg Ferrites. *J. Magn. Magn. Mater.* **2018**, *468*, 73–78. [[CrossRef](#)]
- Sathe, R.B.; Narayankar, C.U.; Patil, R.P.; Patil, R.H.; Patil, S.B. Investigation of Structural and Magnetic Properties of Novel Zn-Substituted Ni-Mg Ferrites. *J. Mater. Sci.-Mater. Electron.* **2023**, *34*, 515.
- Ali, M.A.; Khan, M.N.I.; Chowdhury, F.U.Z.; Hossain, M.M.; Rahaman, M.Z.; Hoque, S.M.; Matin, M.A.; Uddin, M.M. Study of Physical Properties Towards Optimizing Sintering Temperature of Y-substituted Mg-Zn Ferrites. *Results Phys.* **2019**, *14*, 102517.
- Jasrotia, R.; Suman; Verma, A.; Verma, R.; Godara, S.K.; Ahmed, J.; Mehtab, A.; Ahmad, T.; Puri, P.; Kalia, S. Photocatalytic Degradation of Malachite Green Pollutant Using Novel Dysprosium Modified Zn-Mg Photocatalysts for Wastewater Remediation. *Ceram. Int.* **2022**, *48*, 29111–29120. [[CrossRef](#)]
- Somvanshi, S.B.; Jadhav, S.A.; Khedkar, M.V.; Kharat, P.B.; More, S.D.; Jadhav, K.M. Structural, Thermal, Spectral, Optical and Surface Analysis of Rare Earth Metal Ion (Gd^{3+}) Doped Mixed Zn-Mg Nano-Spinel Ferrites. *Ceram. Int.* **2020**, *46*, 13170–13179. [[CrossRef](#)]
- Mansour, S.F.; Al-Wafi, R.; Abdo, M.A. Zn-Mg-La Nanoferrites for Storage and High Frequency Devices with Augmenting the Photocatalytic Performance. *J. Alloys Compd.* **2020**, *826*, 154125. [[CrossRef](#)]
- Jasrotia, R.; Kumari, N.; Verma, R.; Suman; Godara, S.K.; Ahmed, J.; Alshehri, S.M.; Pandit, B.; Thakur, S.; Himanshi; et al. Effect of Rare Earth (Nd^{3+}) Metal Doping on Structural, Morphological, Optical and Magnetic Traits of Zn-Mg Nano-Ferrites. *J. Rare Earths*, 2022; *in press*. [[CrossRef](#)]
- Mansour, S.F.; Wageh, S.; Al-Wafi, R.; Abdo, M.A. Enhanced Magnetic, Dielectric Properties and Photocatalytic Activity of Doped Mg-Zn Ferrite Nanoparticles by Virtue of Sm^{3+} Role. *J. Alloys Compd.* **2021**, *856*, 157437. [[CrossRef](#)]
- Jasrotia, R.; Suman; Verma, A.; Verma, R.; Ahmed, J.; Godara, S.K.; Kumar, G.; Mehtab, A.; Ahmad, T.; Kalia, S. Photocatalytic Dye Degradation Efficiency and Reusability of Cu-Substituted Zn-Mg Spinel Nanoferrites for Wastewater Remediation. *J. Water Process Eng.* **2022**, *48*, 102865. [[CrossRef](#)]
- Mansour, S.F.; Abdo, M.A.; El-Dek, S.I. Improvement of Physico-Mechanical Properties of Mg-Zn Nanoferrites via Cr^{3+} Doping. *J. Magn. Magn. Mater.* **2017**, *422*, 105–111. [[CrossRef](#)]
- Haralkar, S.J.; Kadam, R.H.; More, S.S.; Shirsath, S.E.; Mane, M.L.; Patil, S.; Mane, D.R. Substitutional Effect of Cr^{3+} Ions on the Properties of Mg-Zn Ferrite Nanoparticles. *Phys. B: Condensed Matter* **2012**, *407*, 4338–4346. [[CrossRef](#)]

18. Zhang, W.; Yu, X.; Li, H.; Dong, D.; Zuo, X.; Wu, C. Magnetic Nanoparticles with Low Curie Temperature and High Heating Efficiency for Self-regulating Temperature Hyperthermia. *J. Magn. Magn. Mater.* **2019**, *489*, 165382. [[CrossRef](#)]
19. Yu, X.; Ding, S.; Yang, R.; Wu, C.; Zhang, W. Research Progress on Magnetic Nanoparticles for Magnetic Induction Hyperthermia of Malignant Tumor. *Ceram. Int.* **2021**, *47*, 5909–5917. [[CrossRef](#)]
20. Xia, A.; Liu, S.; Jin, C.; Chen, L.; Lv, Y. Hydrothermal $Mg_{1-x}Zn_xFe_2O_4$ spinel ferrites: Phase formation and mechanism of saturation magnetization. *Mater. Lett.* **2013**, *105*, 199–201. [[CrossRef](#)]
21. Yu, X.; Yang, R.; Wu, C.; Zhang, W. Effect of Chromium Ion Substitution of ZnCo Ferrites on Magnetic Induction Heating. *J. Alloys Compd.* **2020**, *830*, 154724. [[CrossRef](#)]
22. Zhang, W.; Zuo, X.; Niu, Y.; Wu, C.; Wang, S.; Guan, S.; Silva, S.R.P. Novel Nanoparticles with Cr^{3+} Substituted Ferrite for Self-Regulating Temperature Hyperthermia. *Nanoscale* **2017**, *9*, 13929–13937. [[CrossRef](#)] [[PubMed](#)]
23. Priya, G.V.; Murali, N.; Raju, M.K.; Krishan, B.; Parajuli, D.; Choppa, P.; Narayana, P.L. Influence of Cr^{3+} Substituted NiZnCo Nano-ferrites: Structural, Magnetic and DC electrical resistivity properties. *Appl. Phys. A* **2022**, *128*, 663. [[CrossRef](#)]
24. Agrawal, S.; Parveen, A.; Azam, A. Structural, Electrical, and Optomagnetic Tweaking of Zn Doped $CoFe_{2-x}Zn_xO_{4-\delta}$ Nanoparticles. *J. Magn. Magn. Mater.* **2016**, *414*, 144–152. [[CrossRef](#)]
25. Tang, B.; Wang, G.; Zhuo, L.; Ge, J.; Cui, L. Facile Route to α -FeOOH and α -Fe₂O₃ Nanorods and Magnetic Property of α -Fe₂O₃ Nanorods. *Inorg. Chem.* **2006**, *45*, 5196–5200. [[CrossRef](#)] [[PubMed](#)]
26. Almeida, T.P.; Fay, M.; Zhu, Y.; Brown, P.D. Process Map for the Hydrothermal Synthesis of α -Fe₂O₃ Nanorods. *J. Phys. Chem. C* **2009**, *113*, 18689–18698. [[CrossRef](#)]
27. Pankhurst, Q.A.; Connolly, J.; Jones, S.K.; Dobson, J. Applications of Magnetic Nanoparticles in Biomedicine. *J. Phys. D-Appl. Phys.* **2003**, *36*, R167–R181. [[CrossRef](#)]
28. Mmesesi, O.K.; Masunga, N.; Kuvarega, A.; Nkambule, T.T.; Mamba, B.B.; Kefeni, K.K. Cobalt Ferrite Nanoparticles and Nanocomposites: Photocatalytic, Antimicrobial Activity and Toxicity in Water Treatment. *Mater. Sci. Semicond. Process.* **2021**, *123*, 105523. [[CrossRef](#)]
29. Mahajan, H.; Godara, S.K.; Srivastava, A.K. Synthesis and Investigation of Structural, Morphological, and Magnetic Properties of the Manganese Doped Cobalt-Zinc Spinel Ferrite. *J. Alloys Compd.* **2022**, *896*, 162966. [[CrossRef](#)]
30. Himakar, P.; Murali, N.; Parajuli, D.; Veeraiah, V.; Samatha, K.; Mammo, T.W.; Batoo, K.M.; Hadi, M.; Raslan, E.H.; Adil, S.F. Magnetic and DC Electrical Properties of Cu Doped Co–Zn Nanoferrites. *J. Electron. Mater.* **2021**, *50*, 3249–3257. [[CrossRef](#)]
31. Yu, X.; Yang, R.; Wu, C.; Liu, B.; Zhang, W. The Heating Efficiency of Magnetic Nanoparticles under an Alternating Magnetic Field. *Sci. Rep.* **2022**, *12*, 16055. [[CrossRef](#)]
32. Haik Dunn, I.; Jacobo, S.E.; Bercoff, P.G. Structural and Magnetic Influence of Yttrium-For-Iron Substitution in Cobalt Ferrite. *J. Alloys Compd.* **2017**, *691*, 130–137. [[CrossRef](#)]
33. Josephson, L.; Lewis, J.; Jacobs, P.; Hahn, P.F.; Stark, D.D. The Effects of Iron Oxides on Proton Relaxivity. *Magn. Reson. Imaging* **1988**, *6*, 647–653. [[CrossRef](#)] [[PubMed](#)]
34. Zhou, Z.; Yang, L.; Gao, J.; Chen, X. Structure-Relaxivity Relationships of Magnetic Nanoparticles for Magnetic Resonance Imaging. *Adv. Mater.* **2019**, *31*, 1804567. [[CrossRef](#)] [[PubMed](#)]
35. Yang, L.; Wang, Z.; Ma, L.; Li, A.; Xin, J.; Wei, R.; Lin, H.; Wang, R.; Chen, Z.; Gao, J. The Roles of Morphology on the Relaxation Rates of Magnetic Nanoparticles. *ACS Nano* **2018**, *12*, 4605–4614. [[CrossRef](#)]
36. Chavhan, G.B.; Babyn, P.S.; Thomas, B.; Shroff, M.M.; Haacke, E.M. Principles, Techniques, and Applications of T2*-Based MR Imaging and Its Special Applications. *RadioGraphics* **2009**, *29*, 1433–1449. [[CrossRef](#)] [[PubMed](#)]
37. Jiang, Q.L.; Zheng, S.; Hong, R.Y.; Deng, S.Z.; Guo, L.B.; Hu, R.-H.; Gao, B.; Huang, M.; Cheng, L.; Liu, G.-R.; et al. Folic Acid-Conjugated Fe₃O₄ Magnetic Nanoparticles for Hyperthermia and MRI in Vitro and in Vivo. *Appl. Surf. Sci.* **2014**, *307*, 224–233. [[CrossRef](#)]
38. Li, Z.; Wang, S.X.; Sun, Q.; Zhao, H.L.; Lei, H.; Lan, M.B.; Cheng, Z.X.; Wang, X.L.; Dou, S.X.; Max Lu, G.Q. Ultrasmall Manganese Ferrite Nanoparticles as Positive Contrast Agent for Magnetic Resonance Imaging. *Adv. Healthc. Mater.* **2013**, *2*, 958–964. [[CrossRef](#)]
39. Yang, R.; Yu, X.; Li, H.; Wang, C.; Wu, C.; Zhang, W.; Guo, W. Effect of Mg Doping on Magnetic Induction Heating of Zn-Co Ferrite Nanoparticles. *J. Alloys Compd.* **2021**, *851*, 156907. [[CrossRef](#)]
40. Shatooti, S.; Mozaffari, M.; Reiter, G.; Zahn, D.; Dutz, S. An Investigation on the Heat Dissipation in Zn-Substituted Magnetite Nanoparticles, Coated with Citric Acid and Pluronic F127 for Hyperthermia Application. *Phys. B* **2022**, *625*, 413468. [[CrossRef](#)]
41. Li, Z.; Kawashita, M.; Araki, N.; Mitsumori, M.; Hiraoka, M.; Doi, M. Magnetite Nanoparticles with High Heating Efficiencies for Application in the Hyperthermia of Cancer. *Mater. Sci. Engin. C* **2010**, *30*, 990–996. [[CrossRef](#)]
42. Ranoo, S.; Lahiri, B.B.; Damodaran, S.P.; Philip, J. Tuning Magnetic Heating Efficiency of Colloidal Dispersions of Iron Oxide Nano-Clusters by Varying the Surfactant Concentration during Solvothermal Synthesis. *J. Mol. Liq.* **2022**, *360*, 119444. [[CrossRef](#)]

Disclaimer/Publisher's Note: The statements, opinions and data contained in all publications are solely those of the individual author(s) and contributor(s) and not of MDPI and/or the editor(s). MDPI and/or the editor(s) disclaim responsibility for any injury to people or property resulting from any ideas, methods, instructions or products referred to in the content.